Enhancing Millimeter-Wave Computational Interferometric Imaging

SANA ABID[ID], CYRIL DECROZE, MOCTAR MOUHAMADOU, AND THOMAS FROMENTEZE[ID]
XLIM, University of Limoges, UMR CNRS 7252, 87000 Limoges, France

Corresponding author: Sana Abid (sana.abid@unilim.fr)

ABSTRACT Recently a progress in computational imaging has been noticed with the potential to improve the capabilities of millimeter-wave imaging systems. In this paper, an interferometric synthetic aperture systems is considered to be the conventional approach to image reconstruction that, in order to overcome its cost limitations and system complexity, both hardware and digital post-processing solutions are offered. A passive multiplexing cavity is added to encode received signals into the physical layer helping to reduce the number of measurement ports and thus the active RF chains without affecting the initial number of receiving antennas. This proposed technique leads to inverse problem solving process. A novel numerical method is then developed, based on a matrix formalism yielding a mathematical description of the computational approach. A numerical study is therefore performed to approve the feasibility of this technique for a better image reconstruction followed by an experimental study carried out at 92 GHz as a proof of concept.

INDEX TERMS Computational imaging, millimeter-wave sensing, passive coding device, radiometry, synthetic aperture.

I. INTRODUCTION

Under the impetus of many recent technological advances, passive microwave and millimeter wave imaging has found numerous applications in several disciplines. Initially focused on far field applications such as radio astronomy and satellite remote sensing (notably applied to oceanography and meteorology) [1]–[5], this field has then emerged in short range imaging applications such as medical diagnosis [6] and concealed threat detection. Passive millimeter-wave imaging seems to be robust against bad visibility conditions (through clothing, fogs, rain) and suitable for safety applications that respect privacy. Therefore, many millimeter wave radiometers and sensors including SPO-NX QinetiQ [7], TAC-camera (ThruVision), the Millivision imaging system X350 and MM-IMAGER 90 (Mc2 technologies) [8] reveal that researchers and companies have been interested to millimeter wave imaging technology for detecting suspicious object hidden beneath clothing that can be used in the entrances to airports, train stations, malls, sports arenas and other areas to ensure more secure environments. Radiometry

The associate editor coordinating the review of this manuscript and approving it for publication was Stefania Bonafoni[ID].
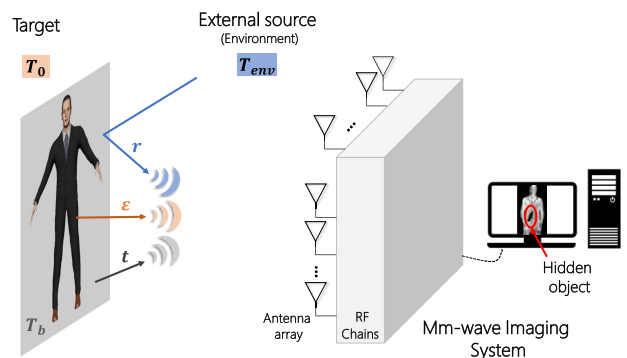

FIGURE 1. Concept of passive imaging corresponding to the measurement of the radiometric temperature T_R.

is a non-invasive technique that measures the thermal electromagnetic radiation of hot objects. One should note that the radiometric temperature T_R does not only depend on the apparent temperature of the imaged object, noted T_0, but it also includes contributions from the background and environmental temperature, noted respectively T_b and T_{env}, that can both be transmitted and reflected by the target (Fig. 1).

$$T_R = \epsilon\, T_0 + r\, T_{env} + t\, T_b \qquad (1)$$

The properties of emissivity ϵ, reflectance r and transmittance t make it possible to classify different materials such as metals and plastics [9]. In the specific case of body scanners, the W-band provides remarkable contrasts between metals exhibiting high reflectivity and human skin being strongly emissive, respectively defined radiometrically cold and hot [10], [11]. This frequency band also benefits from low atmospheric absorption and the millimeter scale dimensions of the wavelengths in play allow both low Rayleigh resolution limits to be reached and systems with a small footprint to be available [12].

There are many different imaging techniques that are distinguished by their way of scanning space and by the associated digital processing. Imaging can for example be achieved by mechanically steering a high gain antenna [13] or by performing a similar operation with the use of a static radiating aperture scanning the space electronically [14], [15].

A great interest has been shown in the development of the technology of Synthetic Aperture Interferometric Radiometer (SAIR) providing high resolution capability and real time acquisitions, thus limiting the use of any mechanical scanning. The single high gain antenna is replaced in this context by a set of small size antenna arranged in an optimized antenna array shape. By adopting an architecture based on the digitization of all the signals received by the array, this approach offers the advantage of being able to form larger effective apertures by cross-correlating all received signals in pairs. Such a technique not only makes it possible to optimize the spatial diversity of the measured information, but it also offers a significant flexibility on image reconstructions by transferring the whole process to the digital layer.

However, this technique requires the use of as many receiving chains as there are antennas forming the radiating aperture [15], imposing high complexity and cost constraints that are prohibitive for many applications. In this context, optimizing the noise level of receivers represents an important challenge to promote the measurement of low-power signals in noisy environments, imposing a new constraint on the multiple reception channels. These systems therefore require an improvement in the sensitivity of each receiver, slowing down the development of this technique for passive imaging.

To overcome these limitations, computational techniques were implemented to reduce the number of active chains required for interferometric imaging systems by adding various types of components for encoding signals into the physical layer quoting code-modulated arrays [16], frequency dispersive reflectarray antennas [17], dynamic metasurfaces [18] and electrically large metallic multiplexing cavities [19]–[23]. The latter is based on the use of passive coding devices initially developed in the microwave domain and then adapted to the millimeter wave range [24]–[26].

However, this computational method is generally dealing with the inversion operation of ill-posed problems since multiplexed SAIR measurement is used to reconstruct the temperature brightness maps. The challenge is therefore about optimizing the post-processing algorithm in order to achieve better image reconstructions with very low false alarms rate and with reasonable computation time. To this end, a mathematical model has already been presented in these works [27], [28] for interferometric systems developed for far-field applications. In this article, the matrix-based formalism is adapted for short range systems where a computational approach is also considered involving a numerical study of achievable performances, as well as an experimental demonstration at W-band of noise sources localization.

II. MATRIX FORMALISM FOR COMPUTATIONAL INTERFEROMETRIC IMAGING

The conventional approach of computational interferometric imaging is first discussed. This principle is illustrated in Fig. 2 where m antennas are connected to the front end of the electrically large cavity as a coding device. The received signals, picked up by the antenna array, are encoded in the physical layer and multiplexed within n output signals where $m \ll n$ by exploiting its high modal diversity. Note that for better image reconstructions, the pseudo-orthogonality of the transfer functions H_{nm} is needed to guarantee sufficiently decorrelated measurements. The cavity responses can be defined as a random Gaussian distributions $n(t) \sim \mathcal{N}(0, \sigma^2)$ exponentially decaying in the time domain due to cavity losses (mainly due to aperture coupling and ohmic losses) which is represented by a decay time τ_{rc} in the following expression [29]:

$$h_{i,j}(\mathbf{t}) = \left(n_{i,j}(\mathbf{t}) \exp(-\frac{\mathbf{t}}{2\,\tau_{rc}}) \right) \qquad (2)$$

where the i, j indexes corresponds to input and output port indices identifying the cavity channels. Maximizing the decay time limits the level of correlation between the impulse responses of the cavity, a phenomenon which is reflected in the frequency domain by a reduction in modal degeneration. The more the excited modes are decorrelated within the cavity, the higher its quality factor is. Motivated by a characterization of the average width of the different frequency resonances in the band of interest, the electromagnetic compatibility range defines the composite quality factor Q as follows [29]:

$$Q = 2\pi f_c \tau_{rc} \qquad (3)$$

where f_c is the central frequency of the operating bandwidth. The cavity is designed using *CST MWS* simulations in order
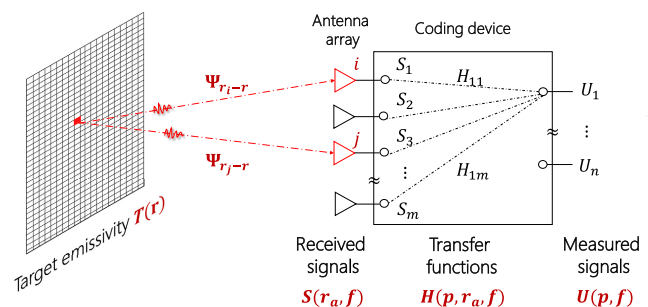
FIGURE 2. Synoptic of the computational interferometric imaging system.

to obtain a statistical prediction of the achievable performances, wishing to optimize the compromise between quality factor and radiation efficiency [30].

Cavity boundary conditions also play a major role in the spatial distribution of modes that defines the coupling to all output ports and thus the level of correlation between its different transfer functions. A cavity with a combination of regular and convex walls results in a geometry qualified as nonintegrable, which ensures a more uniform spatial distribution of modes throughout the useful frequency band [31]. The fixed number of modes determined primarily by the volume of the cavity (as defined by Weyl's law [32]) can thus be optimally exploited to encode spatial information into the frequency domain.

The aim of computational imaging in the microwave and millimeter wave range is thus based on the simplification of the active systems conventionally used, generally employing encoding and multiplexing operations of the information to be measured in order to limit the complexity of the active architectures. The load is then transferred to the digital layer, performing calculations using computers that are becoming increasingly powerful and affordable.

The general principle of the studied interferometric imaging system is presented in Fig. 2.

This passive imaging system interrogates the radiometric temperature $T(\mathbf{r})$ of the region of interest, sliced for reconstruction into a set of pixels or voxels at the resolution limit. The thermal radiation of the target is modeled by a set of sources emitting spatially and temporally incoherent Gaussian-distributed noises. Each of these sources actually corresponds to the superposition at the atomic scale of multiple spontaneous emission processes whose sum forms zero mean signals of power (i.e. variance $\sigma(\mathbf{r})^2$) directly proportional to the apparent temperature of the target:

$$T(\mathbf{r}) \propto \sigma(\mathbf{r})^2 \qquad (4)$$

A target placed in the region of interest $\mathbf{r}$ continuously emits thermal signals $\rho_k(\mathbf{r}, t)$ corresponding to Gaussian-distributed random vectors:

$$\rho_k(\mathbf{r}, t) \sim \mathcal{N}(0, \; \sigma(\mathbf{r})^2) \qquad (5)$$

Each measure of k-index is expressed in the frequency domain with a Fourier transform:

$$\rho_k(\mathbf{r}, \mathbf{f}) = \mathfrak{F}\big(\rho_k(\mathbf{r}, \mathbf{t})\big) \qquad (6)$$

These signals are then propagated from target space $\mathbf{r}$ to the receiving antennas of locations $\mathbf{r_a}$ by means of Green's functions $\Psi_f(\mathbf{r_a}, \mathbf{r})$ defined in free space as:

$$\Psi_f(\mathbf{r_a}, \mathbf{r}) = \frac{\exp\left(-j\frac{2\pi f}{c}|\mathbf{r} - \mathbf{r_a}|\right)}{4\pi |\mathbf{r} - \mathbf{r_a}|} \qquad (7)$$

The signals received by the antennas $S_{f,k}(\mathbf{r_a})$ for each acquisition k take the following form after propagation:

$$S_{f,k}(\mathbf{r_a}) = \int_{\mathbf{r}} \Psi_f(\mathbf{r_a}, \mathbf{r}) \, \rho_{f,k}(\mathbf{r}) \, d^3\mathbf{r} \qquad (8)$$

A conventional system would require as many independent receiving channels as antennas for the measurement of these signals. In the studied context, a component is developed to analogically encode and then multiplex the received signals in a reduced number of acquisitions $u_{f,k}(\mathbf{p})$ on a set of output ports $\mathbf{p}$:

$$U_{f,k}(\mathbf{p}) = \sum_{\mathbf{r_a}} H_f(\mathbf{p}, \mathbf{r_a}) \int_{\mathbf{r}} \Psi_f(\mathbf{r_a}, \mathbf{r}) \, \rho_{f,k}(\mathbf{r}) \, d^3\mathbf{r} \qquad (9)$$

A single operator $M_f(\mathbf{p}, \mathbf{r})$ is then defined in order to highlight the direct link between the apparent temperature of the region of interest and the measured signals:

$$M_f(\mathbf{p}, \mathbf{r}) = \sum_{\mathbf{r_a}} H_f(\mathbf{p}, \mathbf{r_a}) \Psi_f(\mathbf{r_a}, \mathbf{r}) \qquad (10)$$

By a last substitution, a linear relation between the signals measured at each acquisition of index k and those emitted by the target can finally be established as a Fredholm integral equation of the first kind:

$$U_{f,k}(\mathbf{p}) = \int_{\mathbf{r}} M_f(\mathbf{p}, \mathbf{r}) \, \rho_{f,k}(\mathbf{r}) \, d^3\mathbf{r} \qquad (11)$$

An active imaging system could operate solely on the basis of such a model to reconstruct an estimate of the region of interest, exploiting the synchronized radiation of one or multiple emission chains illuminating the scene. In the particular context of a radiometric system having no control over the signals emitted by the target, the random nature of the signals captured at each acquisition does not allow direct reconstruction. Techniques using averaged intensity measurements in the context of computational imaging allow work in a deterministic framework but require discarding relevant phase information [18], [23], [33], [34]. First reconstruction methods have been explored in the microwave range for similar setups [22]. The principle is based on an equalization of the transfer functions of the cavity in order to obtain an estimate of the signals received by the antennas. Their correlation is finally averaged over an acquisition set in order to estimate the so-called visibility functions defined for conventional radiometric systems [35]. It is proposed here to redevelop a complete and rigorous formalism in this context allowing the reconstruction of radiometric images captured by means of computational systems. These developments will make it possible not only to highlight the existing mathematical links between the radiometric temperature of a target and the signals measured on the various ports of the imaging system, but also to dispose of an alternative matrix formalism with increased performance in terms of memory consumption and computing time.

Since one has no control over the thermal signals emitted by the scene to be imaged, it is first of all desirable to calculate a correlation between the different signals measured. In this way, the phase difference between signals reveals the information related to the propagation in free space and then within the cavity. For the continuation of the calculations presented in this section and in order to facilitate

the transposition of the proposed solutions to the numerical domain, discrete formalisms will be proposed. A notation in bold letters is thus maintained for vector quantities, adopting lower case letters for vectors and upper case notations for higher order tensors. A covariance matrix $\mathbf{R}_{\mathbf{u}f}$ is computed by correlating the measured signals $\mathbf{u}_{f,k}$ at each frequency, averaging the results over a set of captures of index k:

$$\mathbf{R}_{\mathbf{u}f} = \langle \mathbf{u}_{f,k} \, \mathbf{u}_{f,k}^{\dagger} \rangle_k \tag{12}$$

Having a set of N_p measurement ports, the covariance matrix at each frequency is of dimension $\mathbb{C}^{N_p \times N_p}$. From the expression of the measured signals given by Eq. (9), it is possible to develop that of their covariance matrix:

$$\mathbf{R}_{\mathbf{u}f} = \mathbf{H}_f \, \boldsymbol{\Psi}_f \, \langle \boldsymbol{\rho}_{f,k} \, \boldsymbol{\rho}_{f,k}^{\dagger} \rangle_k \, \boldsymbol{\Psi}_f^{\dagger} \, \mathbf{H}_f^{\dagger} \tag{13}$$

$$= \mathbf{M}_f \, \mathbf{R}_{\boldsymbol{\rho}f} \, \mathbf{M}_f^{\dagger} \tag{14}$$

where $\mathbf{H}_f \in \mathbb{C}^{N_p \times N_a}$ corresponds to the transfer functions linking the N_p cavity measurement ports to the N_a receiving antennas, $\boldsymbol{\Psi}_f \in \mathbb{C}^{N_a \times N_r}$ corresponds to the Green's functions propagating signals from the N_r pixels of the region of interest to the N_a antennas. According to Eq. (10), $\mathbf{M}_f = \mathbf{H}_f \, \boldsymbol{\Psi}_f$ is the sensing matrix mapping the signals emitted by the target to those measured on the cavity ports. Finally, the development makes it possible to highlight the role of the covariance of the signals emitted by the target, defined as $\mathbf{R}_{\boldsymbol{\rho}f} = \langle \boldsymbol{\rho}_{f,k} \, \boldsymbol{\rho}_{f,k}^{\dagger} \rangle_k$. Exploiting the Gaussian nature of the radiated signals and their spatial orthogonality on the grid defined by the resolution of the imaging system under consideration, the covariance matrix $\mathbf{R}_{\boldsymbol{\rho}f}$ can be greatly simplified. All the diagonal elements correspond to the variances $\sigma(\mathbf{r})^2$ of the different secondary sources forming each pixel of the image, previously identified as proportional to their radiometric temperature. All the off-diagonal entries are negligible as they reflect the averaged level of correlation between different normal random vectors. The expression of $\mathbf{R}_{\boldsymbol{\rho}f}$ can finally be simplified as follows:

$$\mathbf{R}_{\boldsymbol{\rho}\mathbf{f}} = \begin{pmatrix} \sigma_{r_1}^2 & \sigma_{r_1,r_2} & \cdots & \sigma_{r_1,r_N} \\ \sigma_{r_2,r_1} & \sigma_{r_2}^2 & & \vdots \\ \vdots & & \ddots & \vdots \\ \sigma_{r_N,r_1} & \cdots & \cdots & \sigma_{r_N}^2 \end{pmatrix} = \mathrm{diag}(\boldsymbol{\sigma}^2) \tag{15}$$

It is finally possible to express a direct link between the covariance of the measurements at each frequency and the scene in a formalism similar to an eigendecomposition, where the eigenvalues would correspond to the radiometric temperatures interacting with the different eigenvectors forming the non-orthogonal basis set $\mathbf{M}_f$, also referred as sensing matrix:

$$\mathbf{R}_{\mathbf{u}f} = \mathbf{M}_f \, \mathrm{diag}(\boldsymbol{\sigma}^2) \, \mathbf{M}_f^{\dagger} \tag{16}$$

Considering that the relative operating bandwith is low enough to observe no frequency dependency in the radiometric temperatures of the scene, it is possible to propose a formalism that enables all the frequency measurements to be used together for image reconstruction. To this end, the calculation presented in Eq. (16) is first vectorized at each frequency:

$$\mathbf{r}_{\mathbf{u}f} = \mathbf{R}_{\mathbf{M}f} \, \boldsymbol{\sigma}^2 \tag{17}$$

Here, $\mathbf{r}_{\mathbf{u}f} \in \mathbb{C}^{N_p^2 \times 1}$ is the result of the vectorization of $\mathbf{R}_{\mathbf{u}f}$. $\mathbf{R}_{\mathbf{M}f} \in \mathbb{C}^{Np^2 \times N_r}$ is the covariance matrix of each column vector of $\mathbf{M}_f$, reshaped to have dimensions matching the vectorized measurements. $\boldsymbol{\sigma}^2 \in \mathbb{R}^{N_r \times 1}$ is the radiometric temperature of the scene. Finally, this vectorization makes it possible to form by concatenation of the N_f frequency samples a single matrix operator mapping all the correlations of the measurements to the radiometric temperature of the target:

$$\mathbf{r}_{\mathbf{u}} = \mathbf{R}_{\mathbf{M}} \, \boldsymbol{\sigma}^2 \tag{18}$$

where $\mathbf{r}_{\mathbf{u}} \in \mathbb{C}^{N_p^2.N_f \times 1}$ corresponds to the full vector of correlated measurements linked to the space to be imaged by the matrix $\mathbf{R}_{\mathbf{M}} \in \mathbb{C}^{Np^2.N_f \times N_r}$. The radiometric temperature of the scene can finally be estimated by calculating the pseudo-inverse of the $\mathbf{R}_{\mathbf{M}}$ matrix:

$$\hat{\boldsymbol{\sigma}}^2 = \mathbf{R}_{\mathbf{M}}^{+} \, \mathbf{r}_{\mathbf{u}} \tag{19}$$

where $.^{+}$ corresponds to the pseudo-inversion operator. The concatenation of the frequency measurements allows here to increase the amount of information used for the reconstruction of the N_r pixels. The imperfect orthogonality of the cavity transfer and Green functions, however, implies that the $\mathbf{R}_{\mathbf{M}}$ matrix may suffer from conditioning problems. It is therefore necessary for reconstructions to use techniques that do not require magnitude inversion, such as matched filtering, or regularization techniques that limit the magnification of noise subspace. For example, the analogous techniques of Tikohnov regularization or Moore-Penrose pseudo-inversion (truncated SVD) can be implemented to limit these deleterious phenomena.

Summarising, this computational imaging method is based on a formalized matrix resulting from linear combinations of vectors and matrix which leads to the solution of a single inverse problem so called a full matrix approach. The constraint of this method appears when faced to invert large matrices thus consuming a large amount of memory space and slowing down the computation time, which is a major obstacle for real time operation. Faced with these limitations, an alternative way is proposed, exploiting a reconstruction of the images in two stages instead of one. For this approach, it is thus proposed to first estimate the correlation of the signals received by the antennas before interrogating the radiometric temperature of the image from this intermediate information. This proposed reconstruction technique is a factorization of the $\mathbf{R}_{\mathbf{M}}$ matrix into two smaller operators:

$$\mathbf{r}_{\mathbf{u}} \approx \mathbf{R}_{\mathbf{H}} \, \mathbf{R}_{\boldsymbol{\psi}} \, \boldsymbol{\sigma}^2 \tag{20}$$

where $\mathbf{R}_{\mathbf{H}} \in \mathbb{C}^{N_p^2.N_f \times N_a^2}$ stands for the correlation of the cavity transfer functions and $\mathbf{R}_{\boldsymbol{\psi}} \in \mathbb{C}^{N_a^2 \times N_r}$ models the

propagation from the target to the antenna pairs. First of all, it is necessary to define a matrix corresponding only to the correlation of the transfer functions of the cavity. The calculation of the $\mathbf{R_H}$ matrix is carried out at each frequency, for each pair of measuring ports of indices $(i, j) \in \mathbf{p}^2$ and each receiving antenna locations $(r_{a_m}, r_{a_n}) \in \mathbf{r_a}^2$:

$$R_{Hf}(p_i, p_j, r_{a_m}, r_{a_n}) = H_f(p_i, r_{a_m})H_f(p_j, r_{a_n})^* \quad (21)$$

This operator is then reshaped to form the $\mathbf{R_H}$ matrix whose dimensions are specified above. The $\mathbf{R_\psi}$ matrix is formed as follows:

$$R_\psi(r_{a_m}, r_{a_n}, \mathbf{r}) = \Psi_{f_c}(r_{a_m}, \mathbf{r})\Psi_{f_c}(r_{a_n}, \mathbf{r})^* \quad (22)$$

This operator is also reshaped to obtain a matrix of dimensions $\mathbf{R_\psi} \in \mathbb{C}^{N_a^2 \times N_r}$. This factorization is based on an important approximation: exploiting the absence of frequency dependence of the radiometric temperature considering a small fractional bandwidth, it is possible to approximate the propagation operation at the center frequency f_c of the operating bandwidth. Consequently, the reconstruction is carried out in two steps by inverting the two sub-matrices compensating successively for propagation within the cavity and then in free space:

$$\hat{\sigma}^2 \approx \mathbf{R_\psi}^+ \mathbf{R_H}^+ \mathbf{r_u} \quad (23)$$
$$= \mathbf{R_\psi}^+ \hat{\mathbf{V}} \quad (24)$$

where $\hat{\mathbf{V}} = \mathbf{R_H}^+ \mathbf{r_u}$ is the estimation of the visibility matrix, corresponding to the averaged correlation of all the received signals, also known as the visibility functions [35]:

$$V(\mathbf{r_a}, \mathbf{r_a}) = \langle s_f(\mathbf{r_a}) s_f(\mathbf{r_a})^\dagger \rangle_f \quad (25)$$

This intermediate step provides an advantage of interest in creating links between the proposed approach and conventional interferometric systems, most of which are made for operating in Far field with the help of the Van Cittert-Zernike theorem [36]. When working with applications where the distance from the target is of an order of magnitude comparable to that of the aperture formed by the radiating elements, it is however necessary to adapt the formalism initially based on a spatial Fourier transform to the Fresnel zone [37]. Even if this paper focuses only on the use of matrix inversion reconstruction, it is possible to propose an alternative based on Fast Fourier Transforms to the $\mathbf{R_\psi}^+$ matrix.

Similarly to the approaches developed in [20], [24], [38], this work proposes to simplify image reconstructions by using an intermediate step of estimating the correlation of antenna signals. However, the formalism proposed here is distinguished by the use of a fully matrix-based method, in opposition to the previously developed equalization techniques [39]. This new and more rigorous analytical method allows to optimize the quality of the reconstructions by only having matrix inversion operations.

To conclude this section and in summary of the proposed developments, this study has introduced a matrix formalism to clearly show the relationship between the radiometric temperature of a target and the correlation of the signals measured on the ports of a computational imaging system. This first approach is defined as the full operator method. Secondly, it has been possible to propose an approximation based on physical considerations which makes it possible to limit the complexity of the reconstruction by obtaining matrices of reduced dimensions. This second approach, referred to as the factorized operator method, also makes it possible to propose interesting connections with the operation of conventional systems and to exploit the numerical advances made in this context.

III. NUMERICAL STUDY

A numerical study is performed in order to prove the feasibility of the full operator approach as well as the factorized operator, identifying the limitation of the added coding device and the signal processing algorithm. For this study, the image is evaluated using both matrix formalism proposed for the computational technique and then compared to the conventional interferometric method (SAIR). To this end, an imaging scenario is considered where an Y-shaped array constituted of $m = 16$ antennas with 5 antennas per arm in addition to the central one. An inter-element spacing between antennas of $d = 7 \lambda_c$ ($f_c = 92$ GHz) and a distance of $R = 1$ m separating the imaging system to the target leading to a spacial resolution $\delta_x = 1.7$ cm, $\delta_z = 1.97$ cm along x, z axis and a field of view $FOV = 14 \times 14$ cm (with an initial field of view of 8 degrees defined by our sampling conditions, projected over the transverse dimensions at a distance of 1m.). As depicted in Fig. 3, the antenna array is connected to $m \times n$ ports chaotic cavity where n is the number of output ports. The random transfer functions are computed according to Eq. (2) with a time decay $\tau_{rc} = 120$ ns. Since the aim is to reduce the number of output ports, it has therefore been set at $n = 2$. As consequence, it will reduce drastically the measured signals which complicates the image reconstruction. The latter depends on image complexity and the coding device characteristics n and τ_{rc}.

First scenario, a checkerboard and a point source are chosen as the scene to be imaged relative to the amount of information useful to to be determined. A series of simulations, sampled with 6001 frequency points, has been performed within the frequency range $89 - 94$ GHz averaging 100 acquisitions. One should note that the target, represented by a set of spatially incoherent source points emitting value-weighted random Gaussian distribution, is therefore discretized into 32×32 pixels. The scene to be imaged is set in front of an interferometric system of 16 antennas connected to 16×2 cavity (Fig. 3).

The Fig. 4 shows that the checkerboard includes more significant spatial information, thus considering an area more complex than the source point. The estimation of emitted signals for image reconstructions is carried out by solving linear problems with the use of the Tikhonov's regularizations. Theses outcomes are enhanced by optimizing the choice of
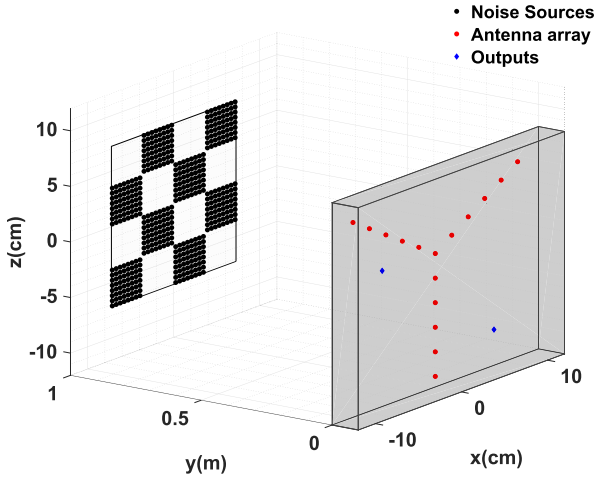
FIGURE 3. The imaging scenario with computational imaging system using a 16 × 2 cavity connected to a Y-shaped antenna array. Notice that a checkerboard, the area to be imaged, is discretized into a set of noise sources.
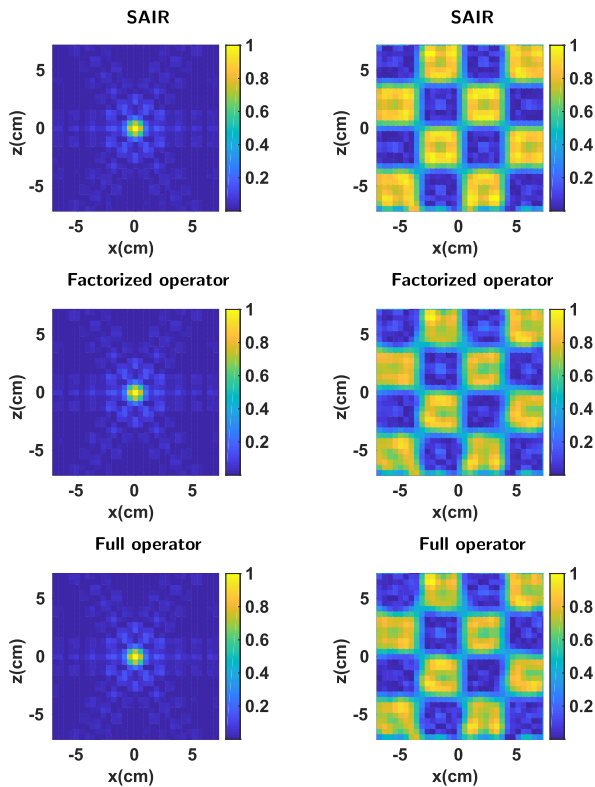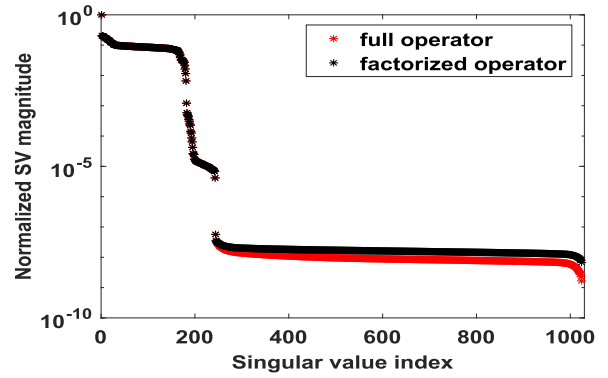

FIGURE 5. The singular value decomposition of both the factorized operator ($R_G = R_H R_\psi$) and the full operator (R_M).

FIGURE 4. Comparison of simulation results of two computational approaches (the full operator approach and the factorized operator approach) as function of the scene to be imaged (checkerboard and point source) with the result obtained by the conventional interferometric approach (SAIR). The magnitudes are normalized.

the regularization parameter. A robustness of the matrix formalism is also revealed for solving linear regression against the amount of spatial information to be determined by illustrating its ability to achieve results comparable to those of the conventional method. Notice that the image quality is reliant to the conditioning of the matrix to be inverted when dealing with computational imaging. An essential parameter to be

taken into account could be fixed from the matrix singular value decomposition (SVD). The Fig. 5 depicts the SVD of both the full and factorized operators that have almost the same result justifying the fact of having a comparable image.

These simulations were conducted with the software *MATLAB* on an operating system with a 3.6 GHz Intel i7 processor and 12 GB of RAM leading to a mean time for image reconstruction, $t_{SAIR} = 6$ ms for the conventional SAIR approach, $t_{R_G} = 24$ ms for the computational technique using the factorized operator and $t_{R_M} = 138$ ms for the computational technique using the full operator. The latter has a slower computation time due to a larger size matrix to be inverted given by $R_M \in \mathbb{C}^{N_p^2 . N_f \times N_r}$ against $\mathbf{R}_\psi \in \mathbb{C}^{N_a^2 \times N_r}$ for SAIR technique and ($\mathbf{R}_\psi \in \mathbb{C}^{N_a^2 \times N_r}$ & $\mathbf{R}_H \in \mathbb{C}^{N_p^2 . N_f \times N_a^2}$) for the factorized operator approach. In addition, the full operator will also require considerable memory space compared to a technique that splits the R_M matrix into two individual operators. It can therefore be concluded that the method based on operator factorization seems to be more favorable for real-time imaging applications.

A further study is carried out evaluating the influence of one of the coding device characteristics. A crucial parameter that highlights the orthogonality of the cavity transfer functions. Adopting the same imaging scenario depicted in Fig. 3 with different time decay ($\tau_{rc} = 120$ ns and $\tau_{rc} = 1$ ns), the Fig. 6 illustrates that the proposed computational approaches with a $\tau_{rc} = 1$ ns fail compared to the previous results with $\tau_{rc} = 120$ ns (Fig. 4) showing that longer the time decay is, better the image reconstruction will be. The energy being enclosed in the cavity for a longer duration reduces the level of correlation of the transfer functions thus improving their orthogonality.

As mentioned previously, an accurate inverse problem solving depends on matrix conditioning. An SVD spectrum of the full operator R_M is then specified in Fig. 7. The full operator with $\tau_{rc} = 120$ ns has SVD with a slow decaying versus a rapid decaying SVD for the case with $\tau_{rc} = 1$ ns reaching rapidly the smallest singular values. So, the matrix conditioning will be damaged deteriorating the image quality subsequently.
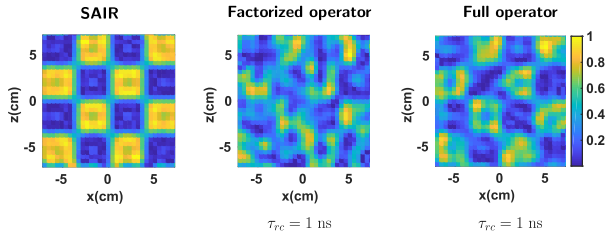
FIGURE 6. Comparison of the simulation results of the proposed approach with the full operator R_M and the factorized operator R_G with a cavity time decay $\tau_{rc} = 1$ ns with the result obtained by the conventional approach. The magnitudes are normalized.
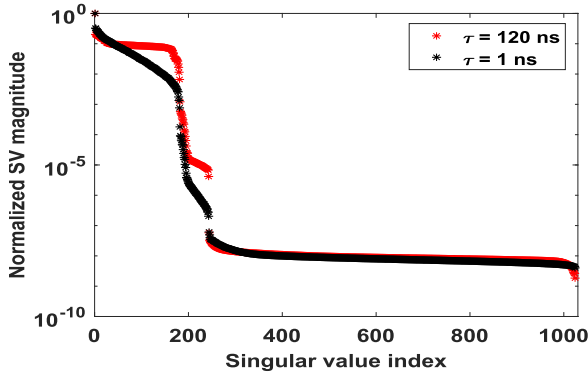

FIGURE 7. The singular value decomposition of the full sensing matrix of the proposed approach (CSAIR R_M) as function of the cavity time decay τ_{rc}.

In contrast to the results with the time decay $\tau_{rc} = 120$ ns, a remarkable difference in image quality reconstructed by the two operators has emerged when time decay turned to $\tau_{rc} = 1$ ns. Since the singular values magnitude decreases faster, a significant noise amplification is induced complicating the setting of an optimized regularization parameter of both matrix to inverse ($\mathbf{R_H}$, $\mathbf{R_\psi}$ from Eq. (23)) to provide accurate and stables solutions which is more attainable for the full operator method leading to a better result.

The study is realised to reveal the influence of digital processing on image reconstruction by offering an optimization-based algorithms that attempt to reduce drastically the RF chains and to minimize the system cost. It could be noticed a robustness of the proposed approaches based on full matrix formalism compared to the conventional interferometric technique. An alternative factorized operator is considered decreasing the computational algorithm complexity without compromising the reconstruction image if a good channels orthogonality is satisfied.

IV. EXPERIMENTAL STUDY

As a proof of concept at W-band, a time-domain millimeter wave imaging system is performed for noise sources localization as depicted in Fig. 8. To this end, the same simulation set up is adopted where 16 horn antennas, arranged in Y-shape, are connected to a 16 to 2 ports electrically large cavity having a volume of $250 \times 250 \times 60$ mm^3.

A noise source, operating over the frequency range $89 - 94$ GHz with a power of up to 10 dBm, is connected
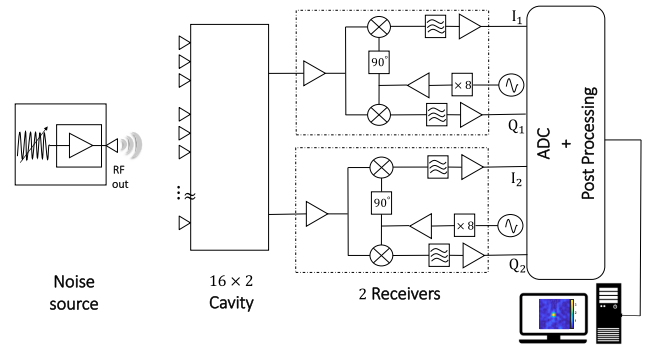

FIGURE 8. Bloc diagram of the experimental imaging system at W-band for noise source localization.

to a 10 dB horn antenna and is used as a point source target (Fig. 9 (a)). The emitted signals are picked up by the receiving waveguide-antenna array (Fig. 9 (b)) then are passively encoded into the physical layer. Signals measured by two receivers operating in W-band (Fig. 9 (c)) undergo IQ demodulation. This operation is performed generating a carrier frequency at 11 GHz up-converted to higher frequencies using x8 multipliers. Two synchronized local oscillators are used in order to limit the impact of phase noise correlation. The baseband signals are then digitized by a 4-channel oscilloscope (Agilent DSA90404A 20 Gsa/s) controlled via an Ethernet connection. For data acquisition, the time duration of the collected signals is 0.5 μs. Eventually, the algorithm proposed above is used to proceed the digital processing for image reconstruction. As a first step, a pre-characterization of the cavity is performed by measuring all the transfer functions to be used later on for the image reconstruction providing the following characteristics: a time decay $\tau_{rc} = 124$ ns, a composite quality factor $Q \approx 75000$ and insertion losses of 27 dB as depicted in Fig 10. The measurement is performed in the frequency domain via a Vector Network Analyzer (VNA) Keysight N5227A in the $89 - 94$ GHz frequency range (with 6001 frequency samples).

The Peak Signal to Noise Ratio *PSNR*, an expression for the ratio between the maximum signal value and the average of measured noise, is the metric used to compare the effects of proposed algorithms on image quality. A series of measurements are carried out once the noise source is maintained in front of the receiving array at a distance $R = 1$ m. The Fig. 11 shows a localization corresponding to the real position of the source as the midpoint of the field of view for both proposed methods. No difference is noticed on image reconstruction as the PSNR is similar $PSNR_{R_G} = 22$ dB and $PSNR_{R_M} = 21$ dB respectively for the full operator and the factorized operator approach. These outcomes reveal that the experimental values are in good agreement with simulation in terms of the spatial resolution evaluated by the full width at a half maximum and the fields of view as there is no aliasing (Tab. 1).
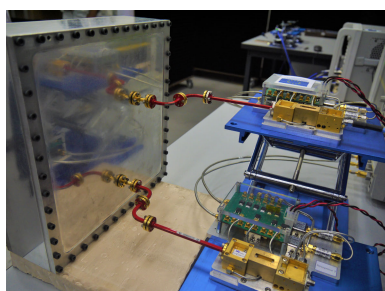
Then, the detection of several noise sources is considered. To this end, the noise source is connected to a chaotic cavity
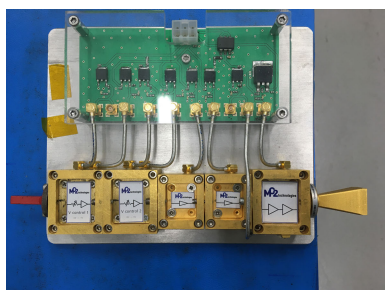
(a)
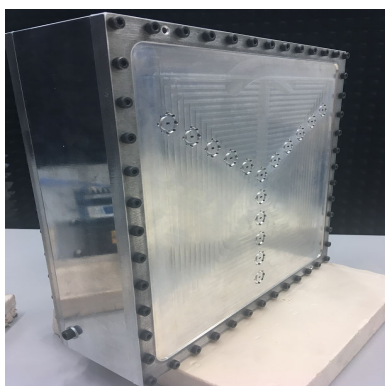
(b)

(c)

FIGURE 9. The measurement bench including the noise source to be localized (a), a 16 × 2 chaotic cavity front view (b), cavity back view connected to 2 receivers (c) manufactured by the company MC2 technologies.
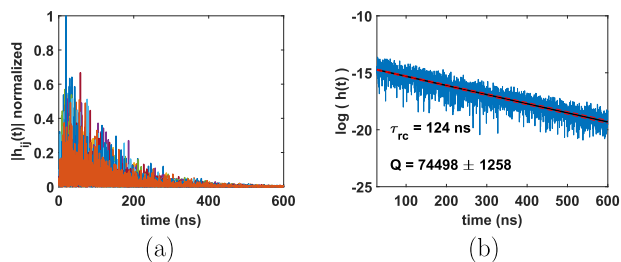

FIGURE 10. Cavity characterization: (a) the impulse response modulus of each channel (b) log-scaled impulse response identifying the decay time τ_{rc} and the corresponding composite quality factor within a margin of error of 2 %.

with a single input and 4 outputs in order to create 4 artificial noise sources and so a simultaneous acquisition of 4 different source locations is possible as depicted in Fig. 12. Considering that the properties of the chaotic cavity have been
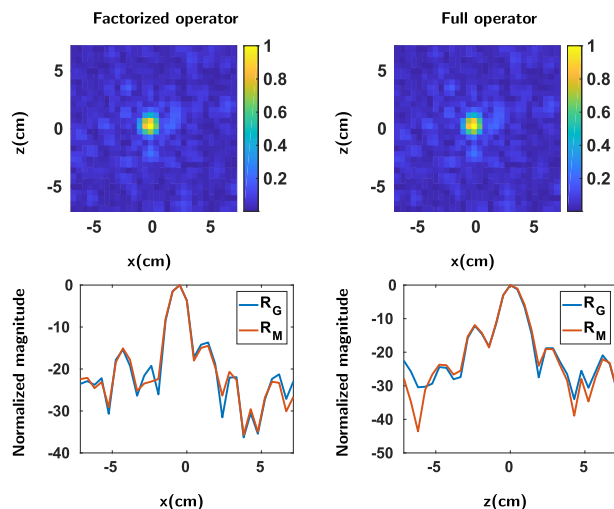

FIGURE 11. Comparison of the experimental imaging results of point-source localization for both proposed approach: with the factorized operator R_G (left) and the full operator R_M (right). The cut planes along the *x* (left) and *z* (right) axes of the reconstructed images by R_G (blue) and R_M (red) operators.

TABLE 1. Comparison of simulation and experimental values.

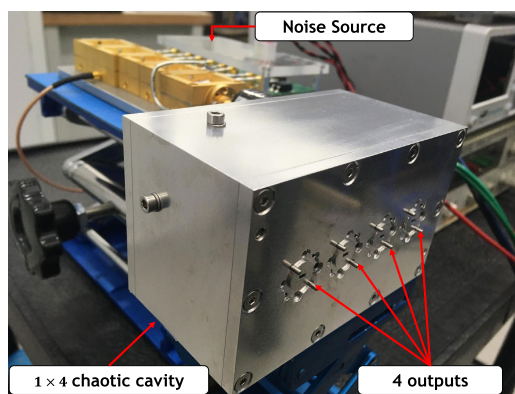|	Simulation	Experimental
Spatial resolution δ_x	1.7 cm	1.44 cm
Spatial resolution δ_z	1.97 cm	1.7 cm
Fields of view FOV	14 cm	15 cm

FIGURE 12. The chaotic cavity with 4 WR-10 waveguides as output ports and a unique input port connected to the noise source to provide location of 4 sources.

evaluated in a previous study [24] ensure that the 4 output signals would be spatio-temporally incoherent signals Eq. (4). The 4 sources, arranged linearly and spaced 2.7 cm each, are positioned in front of the antenna array at a distance of 60 cm leading to the image reconstruction shown in Fig. 13.

Note that the sources do not have the same magnitude, this may be due to a misalignment of the cavity towards the antenna array. Also, the image appears to have a reduced *PSNR* compared to the image of a single source. This comes back to the fact of adding the 1 × 4 cavity which admits insertion losses of 18 dB.
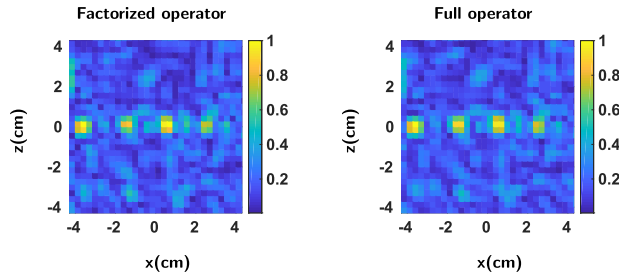
FIGURE 13. Experimental imaging result of 4 sources measured simultaneously thanks to a chaotic cavity.

V. CONCLUSION

A computational imaging system is proposed in this paper. The concept is based on the interferometry principle by adding an oversized cavity to overcome the limitations as the hardware complexity and the cost of the conventional imaging system. A matrix formalism is discussed in the theoretical part thus optimizing the algorithm for image reconstruction. An approach that has been proved to be robust later on by the numerical study, provided that the cavity admits the the satisfying characteristics. A time domain measurement has also being carried out around 90 GHz to approve the feasibility of the imaging system in W-band through noise sources localization. As a future work, incoherent illumination of the scene to be imaged can be considered as a technique to improve contrast and overcome the problem of receiver sensitivity for W-band interferometric imaging systems.

ACKNOWLEDGMENT

REFERENCES

[1] T. T. Wilheit and A. T. C. Chang, "An algorithm for retrieval of ocean surface and atmospheric parameters from the observations of the scanning multichannel microwave radiometer," *Radio Sci.*, vol. 15, no. 3, pp. 525–544, May 1980.

[2] C. S. Ruf, C. T. Swift, A. B. Tanner, and D. M. Le Vine, "Interferometric synthetic aperture microwave radiometry for the remote sensing of the Earth," *IEEE Trans. Geosci. Remote Sens.*, vol. 26, no. 5, pp. 597–611, Sep. 1988.

[3] M. Martín-Neira and J. M. Goutoule, "Miras—A two-dimensional aperture-synthesis radiometer for soil-moisture and ocean-salinity observations," *ESA Bull.*, vol. 92, no. 92, pp. 95–104, Nov. 1997.

[4] D. M. Le Vine, M. Haken, and C. T. Swift, "Development of the synthetic aperture radiometer ESTAR and the next generation," in *Proc. IGARSS-IEEE Int. Geosci. Remote Sens. Symp.*, vol. 2. Sep. 2004, pp. 1260–1263.

[5] I. R. Pérez, "Pau-synthetic aperture: A new instrument to test potential improvements for future interferometric radiometers," Tesi Doctoral, Dept. Teoria Senyal Comunicacions, Univ. Politècnica Catalunya, Barcelona, Spain, 2012.

[6] B. Bocquet, J. C. van de Velde, A. Mamouni, Y. Leroy, G. Giaux, J. Delannoy, and D. Delvalee, "Microwave radiometric imaging at 3 GHz for the exploration of breast tumors," *IEEE Trans. Microw. Theory Techn.*, vol. 38, no. 6, pp. 791–793, Jun. 1990.

[7] N. A. Salmon, "Polarimetric scene simulation in millimeter-wave radiometric imaging," *Proc. SPIE*, vol. 5410, pp. 260–270, Aug. 2004.

[8] E. L. Kpre, N. Vellas, C. Gaquiere, C. Decroze, T. Fromenteze, and M. Mouhamadou, "A compressive millimeter-wave interferometric imager for security applications," in *Proc. IEEE Int. Symp. Antennas Propag. USNC/URSI Nat. Radio Sci. Meeting*, Jul. 2018, pp. 619–620.

[9] N. A. Salmon, R. Appleby, and S. Price, "Scene simulation of passive millimeter-wave images of plastic and metal objects," *Proc. SPIE*, vol. 4719, pp. 397–401, Jul. 2002.

[10] R. Appleby and H. B. Wallace, "Standoff detection of weapons and contraband in the 100 GHz to 1 THz region," *IEEE Trans. Antennas Propag.*, vol. 55, no. 11, pp. 2944–2956, Nov. 2007.

[11] A. Y. Owda, N. Salmon, and N. D. Rezgui, "Electromagnetic signatures of human skin in the millimeter wave band 80-100 GHz," *Prog. Electromagn. Res.*, vol. 80, pp. 79–99, 2018.

[12] J. C. Wiltse, "History of millimeter and submillimeter waves," *IEEE Trans. Microw. Theory Techn.*, vol. 32, no. 9, pp. 1118–1127, Sep. 1984.

[13] Y. Meng, A. Qing, C. Lin, J. Zang, Y. Zhao, and C. Zhang, "Passive millimeter wave imaging system based on helical scanning," *Sci. Rep.*, vol. 8, no. 1, pp. 1–12, Dec. 2018.

[14] D. M. Le Vine, "Synthetic aperture radiometer systems," *IEEE Trans. Microw. Theory Techn.*, vol. 47, no. 12, pp. 2228–2236, Dec. 1999.

[15] S. Vakalis, L. Gong, Y. He, J. Papapolymerou, and J. A. Nanzer, "Experimental demonstration and calibration of a 16-element active incoherent millimeter-wave imaging array," *IEEE Trans. Microw. Theory Techn.*, early access, Apr. 27, 2020, doi: 10.1109/TMTT.2020.2986413.

[16] V. Chauhan, K. Greene, and B. Floyd, "Code-modulated interferometric imaging system using phased arrays," *Proc. SPIE*, vol. 9830, May 2016, Art. no. 98300D.

[17] A. Molaei, G. Allan, J. Heredia, W. Blackwell, and J. Martinez-Lorenzo, "Interferometric sounding using a compressive reflector antenna," in *Proc. 10th Eur. Conf. Antennas Propag. (EuCAP)*, Apr. 2016, pp. 1–4.

[18] A. V. Diebold, M. F. Imani, T. Fromenteze, D. L. Marks, and D. R. Smith, "Passive microwave spectral imaging with dynamic metasurface apertures," *Optica*, vol. 7, no. 5, pp. 527–536, May 2020.

[19] T. Fromenteze, E. L. Kpre, D. Carsenat, C. Decroze, and T. Sakamoto, "Single-shot compressive multiple-inputs multiple-outputs radar imaging using a two-port passive device," *IEEE Access*, vol. 4, pp. 1050–1060, 2016.

[20] E. L. Kpre and C. Decroze, "Synthetic aperture interferometric imaging using a passive microwave coding device," in *Proc. IEEE Conf. Antenna Meas. Appl. (CAMA)*, Oct. 2016, pp. 1–4.

[21] C. Decroze, E. L. Kpre, M. Mouhamadou, T. Fromenteze, and S. Reynaud, "Millimeter wave computational interferometric radiometer," in *Proc. IEEE Int. Symp. Antennas Propag. USNC/URSI Nat. Radio Sci. Meeting*, Jul. 2017, pp. 841–842.

[22] E. L. Kpre and C. Decroze, "Passive coding technique applied to synthetic aperture interferometric radiometer," *IEEE Geosci. Remote Sens. Lett.*, vol. 14, no. 8, pp. 1193–1197, Aug. 2017.

[23] A. C. Tondo Yoya, B. Fuchs, and M. Davy, "Computational passive imaging of thermal sources with a leaky chaotic cavity," *Appl. Phys. Lett.*, vol. 111, no. 19, Nov. 2017, Art. no. 193501.

[24] S. Abid, C. Decroze, T. Fromenteze, and M. Mouhamadou, "Millimeter-wave computational interferometric imaging using a chaotic cavity," in *Proc. IEEE Conf. Antenna Meas. Appl. (CAMA)*, Sep. 2018, pp. 1–4.

[25] T. Zvolensky, V. R. Gowda, J. Gollub, D. L. Marks, and D. R. Smith, "W-band sparse imaging system using frequency diverse cavity-fed metasurface antennas," *IEEE Access*, vol. 6, pp. 73659–73668, 2018.

[26] A. Jouade, S. Meric, O. Lafond, M. Himdi, and L. Ferro-Famil, "A passive compressive device associated with a Luneburg lens for multibeam radar at millimeter wave," *IEEE Antennas Wireless Propag. Lett.*, vol. 17, no. 6, pp. 938–941, Jun. 2018.

[27] G. Hislop and C. Craeye, "On the mathematical link between the MUSIC algorithm and interferometric imaging," *IEEE Trans. Antennas Propag.*, vol. 59, no. 4, pp. 1412–1414, Apr. 2011.

[28] S. Venkatesh, D. Shrekenhamer, W. Xu, S. Sonkusale, W. Padilla, and D. Schurig, "Interferometric direction finding with a metamaterial detector," *Appl. Phys. Lett.*, vol. 103, no. 25, Dec. 2013, Art. no. 254103.

[29] D. A. Hill, *Electromagnetic Fields in Cavities: Deterministic and Statistical Theories*, vol. 35. Hoboken, NJ, USA: Wiley, 2009.

[30] T. Fromenteze, O. Yurduseven, M. F. Imani, J. Gollub, C. Decroze, D. Carsenat, and D. R. Smith, "Computational imaging using a mode-mixing cavity at microwave frequencies," *Appl. Phys. Lett.*, vol. 106, no. 19, May 2015, Art. no. 194104.

[31] C. Draeger, J.-C. Aime, and M. Fink, "One-channel time-reversal in chaotic cavities: Experimental results," *J. Acoust. Soc. Amer.*, vol. 105, no. 2, pp. 618–625, Feb. 1999.

[32] W. Arendt, R. Nittka, W. Peter, and F. Steiner, "Weyl's law: Spectral properties of the Laplacian in mathematics and physics," in *Mathematical Analysis of Evolution, Information, and Complexity*. Hoboken, NJ, USA: Wiley, 2009, ch. 1, pp. 1–71.

[33] T. Fromenteze, X. Liu, M. Boyarsky, J. Gollub, and D. R. Smith, "Phase-less computational imaging with a radiating metasurface," *Opt. Express*, vol. 24, no. 15, pp. 16760–16776, 2016.

[34] A. V. Diebold, M. F. Imani, T. Sleasman, and D. R. Smith, "Phaseless computational ghost imaging at microwave frequencies using a dynamic metasurface aperture," *Appl. Opt.*, vol. 57, no. 9, pp. 2142–2149, 2018.

[35] E. Anterrieu, "A resolving matrix approach for synthetic aperture imaging radiometers," *IEEE Trans. Geosci. Remote Sens.*, vol. 42, no. 8, pp. 1649–1656, Aug. 2004.

[36] F. Zernike, "The concept of degree of coherence and its application to optical problems," *Physica*, vol. 5, no. 8, pp. 785–795, Aug. 1938.

[37] J. Chen, Y. Li, J. Wang, Y. Li, and Y. Zhang, "An accurate imaging algorithm for millimeter wave synthetic aperture imaging radiometer in near-field," *Prog. Electromagn. Res.*, vol. 141, pp. 517–535, 2013.

[38] T. Fromenteze, C. Decroze, S. Abid, and O. Yurduseven, "Sparsity-driven reconstruction technique for microwave/millimeter-wave computational imaging," *Sensors*, vol. 18, no. 5, p. 1536, May 2018.

[39] T. Fromenteze, E. L. Kpre, C. Decroze, D. Carsenat, O. Yurduseven, M. Imani, J. Gollub, and D. R. Smith, "Unification of compressed imaging techniques in the microwave range and deconvolution strategy," in *Proc. Eur. Radar Conf. (EuRAD)*, Sep. 2015, pp. 161–164.

SANA ABID received the master's degree in high-frequency electronics from the University of Limoges, Limoges, France, in 2017, where she is currently pursuing the Ph.D. degree in high-frequency electronics and systems. Her research interests include millimeter-wave imaging and signal processing for computational radiometric imaging.
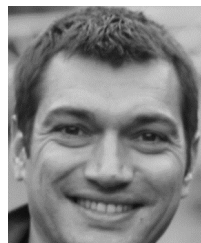
CYRIL DECROZE received the Ph.D. degree in telecommunications engineering from the University of Limoges, Limoges, France, in 2002. He is currently an Associate Professor with the XLIM Research Institute, and obtained the accreditation to direct research (HDR), in December 2013. Since 2016, he has been the Head of the Antennas and Signal Team, XLIM. From 2015 to 2019, he was the Coordinator of the PIXEL Project on millimeter waves interferometric imaging systems, and funded by the French National Research Agency. He has been involved in more than 25 research projects at the national and European levels, and has co-supervised 15 Ph.D. theses. He has coauthored more than 80 peer-reviewed journal articles and conference papers. His research interests include multiple antennas systems, and associated processing for communications and radar imaging.

MOCTAR MOUHAMADOU received the Ph.D. degree in electronics and telecommunications engineering from the University of Limoges, Limoges, France, in 2007. From 2007 to 2010, he was a Research and Development Engineer with the XLIM Research Institute, University of Limoges. He is currently an Associate Professor with Groupe 3iL, Limoges, and develops his research activities with the XLIM Research Institute. His research interests include microwave and millimeter-wave imaging, multiple input multiple output systems, propagation channel, wireless communications, and signal processing for radar and radiometric imaging.

THOMAS FROMENTEZE received the Ph.D. degree from the University of Limoges, Limoges, France, in 2015. From 2015 to 2016, he was a Postdoctoral Researcher with Duke University, Durham, NC, USA. He is currently a Maître de Conférences (Assistant Professor) with the Xlim Research Institute, University of Limoges. He is also an Adjunct Assistant Professor with the Center for Metamaterials and Integrated Plasmonics, Duke University. His research interests include ultra-wideband microwave and millimeter-wave imaging, wave propagation in complex media, computational/compressive imaging, and the various associated inverse problems. He received the 11th EuRAD Young Engineer Prize during the European Microwave Week 2015.

• • •